

# Efficient Calibration in the rough Bergomi model by Wasserstein distance

Changqing Teng <sup>\*</sup> and Guanglian Li<sup>†</sup>

December 2, 2025

## Abstract

Despite the empirical success in modeling volatility of the rough Bergomi (rBergomi) model, it suffers from pricing and calibration difficulties stemming from its non-Markovian structure. To address this, we propose a comprehensive computational framework that enhances both simulation and calibration. First, we develop a modified Sum-of-Exponentials (mSOE) Monte Carlo scheme which hybridizes an exact simulation of the singular kernel near the origin with a multi-factor approximation for the remainder. This method achieves high accuracy, particularly for out-of-the-money options, with an  $\mathcal{O}(n)$  computational cost. Second, based on this efficient pricing engine, we then propose a distribution-matching calibration scheme by using Wasserstein distance as the optimization objective. This leverages a minimax formulation against Lipschitz payoffs, which effectively distributes pricing errors and improving robustness. Our numerical results confirm the mSOE scheme's convergence and demonstrate that the calibration algorithm reliably identifies model parameters and generalizes well to path-dependent options, which offers a powerful and generic tool for practical model fitting.

**Keywords:** rBergomi model, model calibration, Monte Carlo methods, Wasserstein distance.

## 1 Introduction

Empirical studies across a wide range of financial markets have consistently demonstrated that log-volatility time series exhibit behaviors remarkably similar to fractional Brownian motion (fBM) with Hurst index  $H \approx 0.1$  at any reasonable time scale [13]. This groundbreaking discovery has fundamentally reshaped modern financial modeling and spurred the development of a new generation of rough volatility models. Among these, the rough Bergomi

---

<sup>\*</sup>Department of Mathematics, The University of Hong Kong, Pok Fu Lam Road, Hong Kong. Email: [u3553440@connect.hku.hk](mailto:u3553440@connect.hku.hk).

<sup>†</sup>Corresponding author. Department of Mathematics, The University of Hong Kong, Pok Fu Lam Road, Hong Kong. Email: [lotusli@maths.hku.hk](mailto:lotusli@maths.hku.hk).

(rBergomi) model proposed in [6] stands out for its elegant formulation and remarkable capability to jointly capture the dynamics of both historical and implied volatility surfaces.

The asset price process  $S$  in the rBergomi model on a filtered probability space  $(\Omega, \mathcal{F}, \{\mathcal{F}_t\}_{t \in [0, T]}, \mathbb{Q})$ , with  $\mathbb{Q}$  being a risk-neutral measure, satisfies the following dynamics:

$$dS_t = rS_t dt + S_t \sqrt{V_t} \left( \rho dW_t + \sqrt{1 - \rho^2} dW_t^\perp \right), \quad S_0 = s_0, \quad t \in [0, T], \quad (1.1)$$

where  $s_0$  is the initial price, constant  $r$  is the risk-free interest rate,  $T > 0$  is the time horizon and  $W_t$  together with  $W_t^\perp$  are two independent standard Brownian motions. The variance process  $V_t$  satisfies

$$V_t = \xi_0(t) \exp \left( \eta \sqrt{2H} \int_0^t (t-s)^{H-\frac{1}{2}} dW_s - \frac{\eta^2}{2} t^{2H} \right). \quad (1.2)$$

The model dynamics are characterized by four key parameters  $\boldsymbol{\theta} := (\xi_0(t), H, \rho, \eta)$ , where  $\xi_0(t) := \mathbb{E}^{\mathbb{Q}}[V_t | \mathcal{F}_0]$  is the so-called initial forward variance curve. The Hurst index  $H \in (0, 1/2)$  reflects the regularity of  $V_t$  and underlies the rough volatility process. The correlation coefficient  $\rho \in (-1, 0)$  and  $\eta$  is the volatility-of-volatility.

Despite its empirical success, the practical implementation of the rBergomi model faces substantial computational hurdles. The model's reliance on the fractional kernel

$$K(t) := t^{H-\frac{1}{2}}, \quad (1.3)$$

introduces non-Markovianity and destroys the semimartingale property, thereby invalidating conventional PDE-based pricing methods and the application of the Feynman-Kac theorem. This limitation establishes Monte Carlo simulation as the primary numerical approach for option pricing under the rBergomi model. However, the simulation has significant challenges and the central difficulty lies in the efficient discretization of the Volterra process

$$I_t := \sqrt{2H} \int_0^t K(t-s) dW_s. \quad (1.4)$$

While exact simulation via Cholesky factorization is theoretically feasible [6], its  $\mathcal{O}(n^3)$  computational complexity and  $\mathcal{O}(n^2)$  storage requirements render it practically infeasible for realistic applications, as summarized in Table 1. This computational bottleneck has motivated extensive research into approximate simulation schemes. Bennedsen, Lunde, and Pakkanen [7] developed a hybrid scheme for Brownian semistationary processes that handles the kernel singularity by employing power function approximation near the origin and step functions elsewhere. For the rBergomi model specifically, this approach maintains exact treatment of the singularity. Subsequently, Abi Jaber and El Euch [2], Bayer and Breneis [4], and Zhu et al. [25] pursued Markovian approximations through sum-of-exponentials (SOE) representations, which transforms the problem into simulating a weighted sum of diffusion processes. Rømer [21] combined these approaches in a hybrid multifactor scheme that preserves the kernel's exact behavior for several time steps near the origin while approximating the remainder via SOE.

| Methods                | Kernel approximation<br>near the kernel | remainder     | Storage cost       | Computational complexity |
|------------------------|---|---------------|--------------------|--------------------------|
| Choleksy factorization | Exact                                   | Exact         | $\mathcal{O}(n^2)$ | $\mathcal{O}(n^3)$       |
| Hybrid                 | Exact                                   | Step function | $\mathcal{O}(n)$   | $\mathcal{O}(n \log n)$  |
| Multifactor            | SOE                                     | SOE           | $\mathcal{O}(n)$   | $\mathcal{O}(Nn)$        |
| Hybrid multifactor     | Exact                                   | SOE           | $\mathcal{O}(n)$   | $\mathcal{O}(Nn)$        |

Table 1: Comparison between the Monte Carlo based schemes for the rBergomi model, where  $n$  is the time steps and  $N$  denotes the number of summation terms of exponentials.

Beyond pricing challenges, the calibration of the rBergomi model to market data introduces additional complexities. The standard calibration framework involves solving the following optimization problem:

$$\inf_{\boldsymbol{\theta} \in \Theta} \frac{1}{M} \sum_{j=1}^M \delta \left( P(\boldsymbol{\theta}; \zeta_j), P^{MKT}(\zeta_j) \right), \quad (1.5)$$

where  $\Theta$  is a suitable parametric space,  $\delta$  is the error metric,  $\{\zeta_j\}_{j=1}^M = \{(K_j, T_j)\}_{j=1}^M$  is the set of contract parameters and  $P(\boldsymbol{\theta}; \zeta_j)$  is the price of a European option under rBergomi model:

$$P(\boldsymbol{\theta}; \zeta_j) = \mathbb{E}[e^{-rT_j} h(S_{T_j}(\boldsymbol{\theta}))], \quad (1.6)$$

with the payoff function  $h(\cdot) = (\cdot - K_j)^+$  for the call option and  $h(\cdot) = (K_j - \cdot)^+$  for the put.

This formulation raises two critical issues: the treatment of the function-valued parameter  $\xi_0(t)$  and the choice of the metric  $\delta$ . Conventional approaches typically model the initial forward variance curve as a piecewise constant function [16], though recent work by Baschetti et. al. [3] has demonstrated the effectiveness of generalized Nelson-Siegel models [3] for this purpose. In the past few years, one usually introduces an additional neural network for the searched function to strengthen the modeling capability of the stochastic differential equation (SDE) by hybridizing it with deep learning. For instance, Tong et al. [22] pioneered the parameterization of the time-varying Hurst exponent using neural networks. For the choice of pointwise error metric, the traditional calibration usually uses mean squared error (MSE) and solves

$$\inf_{\boldsymbol{\theta} \in \Theta} \frac{1}{M} \sum_{j=1}^M \left( P(\boldsymbol{\theta}; \zeta_j) - P^{MKT}(\zeta_j) \right)^2. \quad (1.7)$$

This approach suffers from one fundamental limitation that it may overfit to the selected data points and perform poorly on tails of the underlying distribution which are outside of observed strikes. Furthermore, model calibration is not necessarily a convex optimization problem and often leads to multiple local minima. Liu et. al. [19] presented the landscape of MSE for the implied volatility of Heston model, with multiple local minima contained. Elaborate choice of error metric could help to mitigate this issue. Kidger et. al. [18] approach the SDE fitting problem as Wasserstein GANs so that any SDE could be learned in the infinite data limit, as Wasserstein distance admits unique global minima.

**Our contributions.** This work addresses the dual challenges of accurate pricing and robust calibration of the rBergomi model.

First, we propose a modified Sum-of-Exponentials (mSOE) scheme which significantly enhances the simulation accuracy of the rBergomi model. Our approach builds upon the hybrid multifactor framework [21] but introduces crucial modifications in both kernel approximation and simulation methodology. We maintain the kernel’s exact form for the first time step to preserve accuracy near the origin while employing a high-fidelity SOE approximation proposed in [17] for the remainder. Furthermore, we simulate the resulting diffusion processes exactly as Gaussian vectors rather than relying on Euler-type discretizations in [21]. We provide a comprehensive weak error analysis that establishes a direct connection between pricing errors and the  $L^\infty$ -error of kernel approximation, and demonstrate numerically that our scheme achieves stable convergence patterns where standard SOE methods fail, particularly in capturing out-of-the-money volatility smiles.

Second, we develop a novel calibration paradigm based on distributional matching via the Wasserstein-1 distance, motivated by the argument in [10, Section 3]. Departing from conventional pointwise price matching by using the error metrics like MSE, our approach minimizes the distance between model-generated and market-implied distributions of the underlying asset across multiple maturities:

$$\inf_{\boldsymbol{\theta} \in \Theta} \frac{1}{M} \sum_{j=1}^M W_1(S_{T_j}(\boldsymbol{\theta}), S_{T_j}^{MKT}),$$

which could cover the information not carried by the selected market data points. Through the Kantorovich-Rubinstein duality [23], the above calibration criterion could be represented as

$$\inf_{\boldsymbol{\theta} \in \Theta} \frac{1}{M} \sum_{j=1}^M \sup_{\text{Lip}(f) \leq 1} \left| \mathbb{E}[f(S_{T_j}(\boldsymbol{\theta}))] - \mathbb{E}[f(S_{T_j}^{MKT})] \right|, \quad (1.8)$$

where  $\text{Lip}(f)$  stands for the Lipschitz constant of  $f$ . Taking  $f(\cdot) = (\cdot - K_j)^+$ , (1.8) is intricately interconnected with (1.5) by taking  $\delta$  to be the absolute pricing error with a null interest rate  $r$ . This formulation corresponds to an adversarial optimization over all Lipschitz-1 payoff functions. Enabled by our efficient mSOE pricing engine, this methodology produces robust calibrations with remarkable parameter identifiability and demonstrate superior generalization to exotic payoffs, as validated through extensive testing on both European and barrier options. Moreover, the calibration framework provided here is generic that permits any reasonable parameterizations of the model parameter and can be applied to models with an efficient Monte Carlo simulation scheme available.

The rest of the paper is organized as follows. Section 2 details the mSOE simulation scheme and its theoretical foundations. Section 3 presents the complete calibration methodology. We illustrate in Section 4 the numerical performance of the mSOE method and the calibration scheme. Finally, Section 5 concludes with directions for future research. The example code for the mSOE scheme and model calibration are available at the GitHub repository <https://github.com/evergreen1002/Calibration-rBergomi-Wasserstein-1>.

## 2 Simulation of the rBergomi model

In this section, we develop the modified Sum-of-Exponentials (mSOE) scheme to efficiently simulate the rBergomi model defined by (1.1) and (1.2). We consider an equidistant temporal grid  $0 = t_0 < t_1 < \dots < t_n = T$  with step size  $\tau := T/n$  and  $t_i := i\tau$ .

### 2.1 Kernel approximation

The simulation of the Volterra process  $I_t$  in (1.4) leads to the primary computational challenge. Our approximation scheme begins with the Laplace transform of the fractional kernel  $K(t) = t^{H-1/2}$ , which is completely monotone <sup>1</sup>. By Bernstein's theorem [24], it can be expressed as:

$$K(t) = \frac{1}{\Gamma(1/2 - H)} \int_0^\infty e^{-xt} x^{-H-1/2} dx =: \int_0^\infty e^{-xt} \mu(dx), \quad (2.1)$$

where  $\mu(dx) = w(x)dx$ , with  $w(x) = \frac{1}{\Gamma(1/2 - H)} x^{-H-1/2}$ . This establishes that  $K(t)$  is an infinite weighted mixture of exponentials. Applying this to the Volterra process  $I_t$  and invoking the stochastic Fubini theorem yields:

$$\begin{aligned} I_t &= \sqrt{2H} \int_0^\infty \int_0^t e^{-x(t-s)} dW_s \mu(dx) \\ &=: \sqrt{2H} \int_0^\infty Y_t^x \mu(dx), \end{aligned}$$

where for any  $x \geq 0$ ,  $Y_t^x$  is an Ornstein-Uhlenbeck process satisfying  $dY_t^x = -xY_t^x dt + dW_t$  with  $Y_0^x = 0$ . This formulation suggests approximating  $I_t$  by discretizing the integral and using a finite sum of exponentials of the kernel:

$$K^N(t) := \sum_{k=1}^N \omega_k e^{-\lambda_k t}, \quad (2.2)$$

for non-negative nodes  $\{\lambda_k\}_{k=1}^N$  and weights  $\{\omega_k\}_{k=1}^N$ . The theoretical foundation for this approximation is guaranteed by the following theorem, which asserts the existence of exponential convergent SOEs for each completely monotone function.

**Theorem 2.1** ([8, Chapter 6, Theorem 3.4]). *Assume  $g(x)$  is completely monotone and analytic for  $\operatorname{Re}(x) > 0$ , and let  $0 < a < b$ . Then there exists an  $N$ -term SOE  $g^N(x) := \sum_{k=1}^N \omega_k e^{-\lambda_k x}$  on the interval  $[a, b]$  such that*

$$\lim_{N \rightarrow \infty} \|g - g^N\|_{C([a,b])}^{1/N} \leq \sigma^{-2}.$$

Here,  $\sigma = \exp\left(\frac{\pi \mathcal{K}(k)}{\mathcal{K}(k')}\right)$  with  $k = \frac{a}{b}$ ,  $k' = \frac{\sqrt{b^2 - a^2}}{b}$  and  $\mathcal{K}(k)$  the complete elliptic integral of the first kind with modulus  $k$ .

---

<sup>1</sup>A function  $g(x)$  is completely monotone if it satisfies  $(-1)^k g^{(k)}(x) \geq 0$  for all  $x > 0$  and  $k = 0, 1, 2, \dots$ .

Since  $K$  is singular at the origin, the approximation  $K^N(t)$ , as stated in the above theorem, is pointwise meaningful on an interval  $[\tau, T]$  with  $\tau > 0$ . Moreover, as  $K$  only appears inside the integrals of  $I_t$ , one could expect that the kernel approximation is valid in some  $L^p([0, T])$  sense for  $p \geq 1$ . For instance, Bayer and Breneis [4] used Gaussian quadrature to achieve a sub-polynomial convergence rate of the  $L^2$ -error. Due to the better integrability property of  $K$  at  $t = 0$  than  $K^2$ , they later proposed in [5] to minimize the  $L^1$ -error with a faster convergence rate. However, for the purpose of model calibration, it is crucial that our kernel approximation permits the computation of gradients with respect to the Hurst index  $H$ . This requirement leads us to adopt the algorithm studied in [17], which combines Gauss-Jacobi and Gauss-Legendre quadrature on geometric-spacing intervals. This scheme effectively controls the  $L^\infty$ -error and, most importantly, enables stable gradient computation that alternative kernel approximation schemes generally fail. In addition, it could work even for the hyper-rough case where  $H \in (-3/2, 0)$ .

To further enhance accuracy by explicitly handling the singularity, we keep the kernel exact for the first time step and approximate the remainder using SOE. There is no discernible accuracy improvement to treat the kernel exact for more than one time step, as shown in [7] and [21]. We thus define our modified kernel approximation as

$$\hat{K}(t) := \begin{cases} t^{H-\frac{1}{2}} & t \in [t_0, t_1), \\ \sum_{k=1}^N \omega_k e^{-\lambda_k t} & t \in [t_1, t_n]. \end{cases} \quad (2.3)$$

## 2.2 Weak Error Analysis

In the sequel, we aim to provide a weak error bound by using the kernel approximation error. We start by rewriting (1.1)-(1.2) as follows

$$\begin{aligned} S_t &= s_0 + \int_0^t rS_s ds + S_s \exp(X_s) dZ_s, \quad Z_s = \rho W_s + \sqrt{1-\rho^2} W_s^\perp, \\ X_t &= \frac{1}{2} \log V_t = \frac{1}{2} \left( \log \xi_0(t) + \eta I_t - \frac{\eta^2}{2} \mathbb{E}[I_t^2] \right). \end{aligned} \quad (2.4)$$

Let  $\hat{S}_t$ ,  $\hat{X}_t$  and  $\hat{I}_t$  be the corresponding process of  $S_t$ ,  $X_t$  and  $I_t$  in (2.4) with  $K$  replaced by  $\hat{K}$ . Observe that the term  $t^{2H}$  in (1.2) corresponds to the square of the  $L^2$ -norm of the Volterra process  $I_t$ . For the numerical simulation, we therefore replace it by the square of the  $L^2$ -norm of its mSOE approximation accordingly. The following lemma is adapted from [15], which bounds the weak error introduced by our approximation.

**Lemma 2.1** ([15, Lemma 3]). *Let  $S, \hat{S}, X, \hat{X} : [0, T] \times \Omega \rightarrow \mathbb{R}$  be continuous stochastic processes satisfying*

$$S_t = s_0 + \int_0^t rS_s ds + S_s \exp(X_s) dZ_s, \quad \hat{S}_t = s_0 + \int_0^t r\hat{S}_s ds + \hat{S}_s \exp(\hat{X}_s) dZ_s,$$

and let  $f : (0, \infty) \rightarrow \mathbb{R}$  be a function such that  $f \circ \exp$  is Lipschitz continuous with Lipschitz constant  $L$ , then there holds

$$\begin{aligned} & \left| \mathbb{E}[f(S_T)] - \mathbb{E}[f(\hat{S}_T)] \right| \\ & \leq L(\sqrt{T} + 6) \left( \mathbb{E} \sup_{t \in [0, T]} \left( \exp(2|X_t|) + \exp(2|\hat{X}_t|) \right)^2 \right)^{1/2} \left( \int_0^T \mathbb{E}[|X_t - \hat{X}_t|^2] dt \right)^{1/2}. \end{aligned} \quad (2.5)$$

Then we derive the weak error between  $S_T$  and  $\hat{S}_T$  due to kernel approximation of  $K(t)$  by  $\hat{K}(t)$ .

**Corollary 2.1.** *Let  $f : (0, \infty) \rightarrow \mathbb{R}$  be a real-valued function such that  $f \circ \exp$  is Lipschitz continuous with Lipschitz constant  $L$ , then there holds*

$$\left| \mathbb{E}[f(S_T)] - \mathbb{E}[f(\hat{S}_T)] \right| \leq C \left( \int_{t_1}^T \left| K(t) - \hat{K}(t) \right|^2 ds \right)^{1/2}. \quad (2.6)$$

Here, the constant  $C$  depends on  $L$ ,  $T$ ,  $\xi_0(t)$ ,  $H$  and  $\eta$ .

*Proof.* First, the definition of  $X_t$  in (2.4) implies

$$X_t - \hat{X}_t = \frac{\eta}{2}(I_t - \hat{I}_t) - \frac{\eta^2}{4}\mathbb{E}[I_t^2 - \hat{I}_t^2].$$

By denoting  $A := \mathbb{E}[I_t^2 - \hat{I}_t^2]$ , and taking the second moment on both sides, this leads to

$$\mathbb{E}[|X_t - \hat{X}_t|^2] = \frac{\eta^2}{4}\mathbb{E}[|I_t - \hat{I}_t|^2] + \frac{\eta^4}{16}A^2.$$

Next, we estimate the two terms on the right hand side. To estimate the first term, an application of the Itô isometry for  $t \in (\tau, T]$  implies

$$\begin{aligned} \mathbb{E}[|I_t - \hat{I}_t|^2] &= 2H \int_0^{t-\tau} |K(t-s) - \hat{K}(t-s)|^2 ds \\ &= 2H \int_{\tau}^t |K(s) - \hat{K}(s)|^2 ds. \end{aligned} \quad (2.7)$$

Note that the second term can be expressed as

$$\begin{aligned} A^2 &= 4H^2 \left| \int_0^t (K(t-s) + \hat{K}(t-s))(K(t-s) - \hat{K}(t-s)) ds \right|^2 \\ &\leq 4H^2 \int_0^t \left| K(t-s) + \hat{K}(t-s) \right|^2 ds \int_0^t \left| K(t-s) - \hat{K}(t-s) \right|^2 ds \\ &\leq 4MH^2 \int_{\tau}^t \left| K(s) - \hat{K}(s) \right|^2 ds, \end{aligned}$$

for some constant  $M$  since both  $K$  and  $\hat{K}$  are square-integrable. Combining these bounds yields

$$\mathbb{E}[|X_t - \hat{X}_t|^2] \leq \left( \frac{1}{2}\eta^2 H + \frac{1}{4}MH^2\eta^4 \right) \int_{\tau}^T |K(s) - \hat{K}(s)|^2 ds.$$

Finally, a combination of integrating over  $[0, T]$  and applying Lemma 2.1 leads to the desired assertion.  $\square$

**Corollary 2.2.** *Let  $f : (0, \infty) \rightarrow \mathbb{R}$  be a real-valued function such that  $f \circ \exp$  is Lipschitz continuous with Lipschitz constant  $L$ . If the kernel approximation (2.3) achieves a uniform precision  $\varepsilon$  over the interval  $[\tau, T]$  with the number of summation terms  $N := N(H, \tau, T, \varepsilon)$ , i.e.,*

$$\sup_{t \in [\tau, T]} |K(t) - \hat{K}(t)| \leq \varepsilon,$$

then the weak error satisfies

$$|\mathbb{E}[f(S_T)] - \mathbb{E}[f(\hat{S}_T)]| \leq C\sqrt{T - \tau}\varepsilon,$$

where the constant  $C$  depends on  $L, T, \xi_0(t), H$  and  $\eta$ .

**Remark 2.1.** *To the best of our knowledge, a general weak convergence result for the rBergomi model with nonlinear payoffs remains an open problem. One of the major hurdles is the moment explosion behavior of the underlying asset at each positive time, as indicated by [12, Theorem 1.2] and [14, Theorem 6.11] in a more general setting.*

### 2.3 mSOE scheme

We now present the complete mSOE scheme for simulating  $(S_{t_i}, V_{t_i})$  on the temporal grid. The Volterra process is decomposed as a summation of the local part and the historical part

$$I_{t_{i+1}} = \underbrace{\sqrt{2H} \int_{t_i}^{t_{i+1}} (t_{i+1} - s)^{H-\frac{1}{2}} dW_s}_{I_{\mathcal{N}}(t_{i+1})} + \underbrace{\sqrt{2H} \int_0^{t_i} (t_{i+1} - s)^{H-\frac{1}{2}} dW_s}_{I_{\mathcal{F}}(t_{i+1})}.$$

Consistent with our kernel approximation  $\hat{K}$ , the local part  $I_{\mathcal{N}}(t_{i+1}) \sim \mathcal{N}(0, \tau^{2H})$  is simulated exactly, and the historical part  $I_{\mathcal{F}}(t_{i+1})$  is approximated via

$$\bar{I}_{\mathcal{F}}(t_{i+1}) = \sqrt{2H} \sum_{k=1}^N \omega_k \int_0^{t_i} e^{-\lambda_k(t_{i+1}-s)} dW_s =: \sqrt{2H} \sum_{k=1}^N \omega_k \bar{I}_{\mathcal{F}}^k(t_{i+1}),$$

where the  $k$ th historical component  $\bar{I}_{\mathcal{F}}^k$  follows the recurrence:

$$\bar{I}_{\mathcal{F}}^k(t_{i+1}) = e^{-\lambda_k \tau} \left( \bar{I}_{\mathcal{F}}^k(t_i) + \int_{t_{i-1}}^{t_i} e^{-\lambda_k(t_i-s)} dW_s \right), \quad i \geq 1,$$

with initialization  $\bar{I}_{\mathcal{F}}^k(t_1) = 0$ . The recurrence requires sampling a centered  $(N + 2)$ -dimensional Gaussian vector at each step

$$\Xi_i := \left( \Delta W_{t_i}, \int_{t_{i-1}}^{t_i} e^{-\lambda_1(t_i-s)} dW_s, \dots, \int_{t_{i-1}}^{t_i} e^{-\lambda_N(t_i-s)} dW_s, I_{\mathcal{N}}(t_i) \right),$$

where  $\Delta W_{t_i} := W_{t_i} - W_{t_{i-1}}$ . The covariance matrix  $\Sigma$  of  $\Xi_i$  has entries

$$\begin{aligned} \Sigma_{1,1} &= \tau, \quad \Sigma_{1,\ell} = \Sigma_{\ell,1} = \frac{1}{\lambda_{\ell-1}} (1 - e^{-\lambda_{\ell-1}\tau}), \quad \Sigma_{k,\ell} = \frac{1}{\lambda_{k-1} + \lambda_{\ell-1}} (1 - e^{-(\lambda_{k-1} + \lambda_{\ell-1})\tau}), \\ \Sigma_{N+2,1} &= \Sigma_{1,N+2} = \frac{\sqrt{2H}}{H+1/2} \tau^{H+\frac{1}{2}}, \\ \Sigma_{N+2,\ell} &= \Sigma_{\ell,N+2} = \frac{\sqrt{2H}}{\lambda_{\ell-1}^{H+1/2}} \gamma(H + \frac{1}{2}, \lambda_{\ell-1}\tau), \\ \Sigma_{N+2,N+2} &= \tau^{2H}, \end{aligned}$$

for  $k, \ell = 2, \dots, N + 1$ , where  $\gamma(\cdot, \cdot)$  refers to the lower incomplete gamma function. Since  $\Sigma$  is time-independent, we only need to implement Cholesky decomposition once. As aforementioned, the term  $\mathbb{E}[I_t^2] = t^{2H}$  in (1.2) is replaced by the second moment of its approximation

$$\mathbb{E} [\bar{I}_{t_i}^2] = \mathbb{E} [(I_{\mathcal{N}}(t_i) + \bar{I}_{\mathcal{F}}(t_i))^2] = \tau^{2H} + 2H \sum_{k,\ell=1}^N \frac{\omega_k \omega_{\ell}}{\lambda_k + \lambda_{\ell}} (e^{-(\lambda_k + \lambda_{\ell})\tau} - e^{-(\lambda_k + \lambda_{\ell})t_i}).$$

Finally, the complete mSOE scheme proceeds as follows for  $i = 0, \dots, n - 1$ :

1. Sample the Gaussian vector  $\Xi_{i+1}$  using the precomputed Cholesky factor.
2. Update historical components:

$$\bar{I}_{\mathcal{F}}^k(t_{i+1}) = e^{-\lambda_k \tau} \left( \bar{I}_{\mathcal{F}}^k(t_i) + \Xi_{i+1}^{(k+1)} \right), \quad k = 1, \dots, N,$$

where  $\Xi_{i+1}^{(k+1)}$  denotes the  $(k + 1)$ th entry of  $\Xi_{i+1}$ .

3. Compute the variance process:

$$\bar{V}_{t_{i+1}} = \xi_0(t_{i+1}) \exp \left( \eta \left( \sqrt{2H} \sum_{k=1}^N \omega_k \bar{I}_{\mathcal{F}}^k(t_{i+1}) + \Xi_{i+1}^{(N+2)} \right) - \frac{\eta^2}{2} \mathbb{E} [\bar{I}_{t_{i+1}}^2] \right).$$

4. Update the asset price process by Euler-Maruyama:

$$\bar{S}_{t_{i+1}} = \bar{S}_{t_i} \exp \left( \left( r - \frac{1}{2} \bar{V}_{t_i} \right) \tau + \sqrt{\bar{V}_{t_i}} \left( \rho \Xi_{i+1}^{(1)} + \sqrt{1 - \rho^2} \Delta W_{t_{i+1}}^{\perp} \right) \right).$$

Computational complexity: The mSOE scheme requires  $\mathcal{O}(N^3)$  offline cost for the Cholesky decomposition and  $\mathcal{O}(Nn)$  online computation with  $\mathcal{O}(N)$  storage per path.

### 3 Calibration scheme

We now present a novel calibration framework for the rBergomi model that fundamentally rethinks the calibration objective by employing the Wasserstein-1 distance as the loss function. We begin by establishing the theoretical foundation of the Wasserstein distance and its relevance to financial model calibration.

#### 3.1 Wasserstein distance

**Definition 3.1.** *Let  $(\mathcal{X}, d)$  be a complete metric space. For any  $p \geq 1$ , the Wasserstein- $p$  distance between two Borel probability measures  $\mu$  and  $\nu$  on  $\mathcal{X}$  is defined by*

$$W_p(\mu, \nu) = \left( \inf_{\gamma \in \Gamma(\mu, \nu)} \mathbb{E}_{(x, y) \sim \gamma} d^p(x, y) \right)^{1/p},$$

where  $\Gamma(\mu, \nu)$  is the set of all Borel probability measures on  $\mathcal{X} \times \mathcal{X}$  with marginals  $\mu$  and  $\nu$ .

Intuitively, the Wasserstein distance measures the minimum work required to transform one probability distribution into another, where the cost of moving mass is proportional to the distance of raised to the power  $p$ . We specialize to the case  $p = 1$  with  $\mathcal{X} = \mathbb{R}$  equipped with the Euclidean metric  $d(x, y) = |x - y|$ . The following theorem shows that for real-valued random variables, the Wasserstein-1 distance admits a tractable representation that bypasses the need for solving the optimal transport problem directly.

**Theorem 3.1** ([9, Theorem 2.1]). *Let  $X$  and  $Y$  be real-valued random variables with cumulative distribution functions  $F_X$  and  $F_Y$ , respectively. The Wasserstein-1 distance between  $X$  and  $Y$  equals the area between their distribution functions:*

$$W_1(X, Y) = \int_{\mathbb{R}} |F_X(u) - F_Y(u)| du = \int_0^1 |F_X^{-1}(z) - F_Y^{-1}(z)| dz,$$

where the quantile function  $F^{-1} : [0, 1] \rightarrow \mathbb{R}$  is defined by

$$F^{-1}(z) := \inf \{u \in \mathbb{R} : F(u) \geq z\}.$$

The quantile function formulation informs the computational approach. In practical applications, we work with empirical distributions derived from samples.

**Definition 3.2.** *Given  $m$  samples from each distribution,  $\{X_i\}_{i=1}^m$  and  $\{Y_i\}_{i=1}^m$ , the empirical Wasserstein-1 distance is defined by*

$$W_1(\{X_i\}, \{Y_i\}) = \frac{1}{m} \sum_{i=1}^m |X_{(i)} - Y_{(i)}|, \quad (3.1)$$

where  $X_{(i)}$  and  $Y_{(i)}$  denote the  $i$ -th order statistics of the samples.

The most profound insight for our calibration methodology comes from an alternative characterization of the Wasserstein-1 distance provided by Kantorovich-Rubinstein duality [23].

**Definition 3.3.** Let  $X, Y$  be two random variables, then the Kantorovich-Rubinstein duality states that

$$W_1(X, Y) = \sup_{\text{Lip}(f) \leq 1} (\mathbb{E}[f(X)] - \mathbb{E}[f(Y)]), \quad (3.2)$$

where  $\text{Lip}(f)$  denotes the Lipschitz constant of  $f$  and  $f : \mathbb{R} \rightarrow \mathbb{R}$ .

This duality result transforms the primal definition into a supremum over a class of test functions, which provides a powerful adversarial interpretation to the calibration approach, as presented in the following subsection.

## 3.2 Calibration via Distributional Matching

Suppose there exists a desirable set of model parameters  $\boldsymbol{\theta}_{\text{true}}$  for the rBergomi model so that the model price perfectly matches the market price, i.e.,

$$P(\boldsymbol{\theta}_{\text{true}}; K, T) = P^{MKT}(K, T), \quad \text{for all } K \text{ and } T. \quad (3.3)$$

However, (3.3) may not have any solutions for two reasons. On the one hand, every model is "mis-specified" to some extent, so the observed option prices may not lie within the range of prices attainable by the model. On the other hand, the observed option prices are "noisy", which are defined up to a bid-ask spread. Conventional model calibration typically minimizes a pointwise discrepancy between model and market prices across a discrete set of options which generally suffers from overfitting. Our framework addresses this limitation by reconceptualizing calibration as distributional matching rather than pointwise price matching. The crucial insight comes from applying the Kantorovich-Rubinstein duality to the option pricing context.

Consider a European option with payoff  $h$ , which is a 1-Lipschitz function of the underlying price. Assume a zero interest rate for simplicity, then the pricing error for this option can be bounded using Definition 3.3:

$$\begin{aligned} |P(\boldsymbol{\theta}; K, T) - P^{MKT}(K, T)| &= |\mathbb{E}[h(S_T(\boldsymbol{\theta}))] - \mathbb{E}[h(S_T^{MKT})]| \\ &\leq W_1(S_T(\boldsymbol{\theta}), S_T^{MKT}) \quad \text{for all } K. \end{aligned} \quad (3.4)$$

This inequality indicates the Wasserstein-1 distance between the model distribution  $S_T(\boldsymbol{\theta})$  and market-implied distribution  $S_T^{MKT}$  provides a uniform bound on pricing errors across all possible strikes for a fixed maturity  $T$ . The duality perspective offers an adversarial interpretation: the Wasserstein-1 distance corresponds to the worst-case pricing error over all 1-Lipschitz payoffs, and implicitly identifies the strike that maximizes the discrepancy between model and market prices. This leads to our proposed calibration objective that minimizes the Wasserstein-1 distance between the model-generated and market-implied distributions across all maturities:

$$\mathcal{L}(\boldsymbol{\theta}) = \frac{1}{M} \sum_{j=1}^M W_1(S_{T_j}(\boldsymbol{\theta}), S_{T_j}^{MKT}). \quad (3.5)$$

To implement this framework, we allow flexible parameterizations of the model parameters  $(\xi_0(t), H, \rho, \eta)$ . Denote

$$\xi_0(t) := \xi_0(t; \boldsymbol{\theta}_\xi), \quad H := \theta_H, \quad \rho := \theta_\rho, \quad \eta := \theta_\eta,$$

with  $\boldsymbol{\theta} := (\boldsymbol{\theta}_\xi, \theta_H, \theta_\rho, \theta_\eta)$  being all the weights of parameterizations and the scalar parameters  $H, \rho, \eta$  are treated as directly trainable weights. In practice, market option prices are quoted with bid-ask spreads. It would be reasonable for a model to retrieve the market price  $P^{MKT}$  with precision not higher than the tolerance level  $|P_{\text{bid}}^{MKT} - P_{\text{ask}}^{MKT}|$ . We therefore define a tolerance level  $\epsilon$  as

$$\epsilon := \frac{1}{M} \sum_{j=1}^M |P_{\text{bid}}^{MKT}(K_j, T_j) - P_{\text{ask}}^{MKT}(K_j, T_j)|, \quad (3.6)$$

and terminate the optimization when  $\mathcal{L}(\boldsymbol{\theta}) \leq \epsilon$ . Besides, the algorithm will be early stopped if the current training loss does not have a substantial improvement compared to the best recorded loss for a certain number of iterations. This number of iterations is termed as "patience" and we denote the minimum tolerable improvement as  $\Delta^{\min}$ .

---

**Algorithm 1** Calibration of rBergomi model by Wasserstein-1 distance

---

**Require:** Time grid  $0 = t_0 < t_1 < \dots < t_n = T$ ;  
 Contract parameter  $\{(K_j, T_j)\}_{j=1}^M$ ;  
 Market-implied samples  $(S_{T_j}^{MKT})_{j=1}^M$ ;  
 Learning rate schedule  $\alpha$ ;  
 Batch size  $m$ ;  
 Tolerance  $\epsilon$  based on bid-ask spreads;  
**Initialization:**  $\boldsymbol{\theta} \leftarrow \boldsymbol{\theta}_0$   
**while**  $\mathcal{L}(\boldsymbol{\theta}) > \epsilon$  or not converge **do**  
**for**  $T_j$  in  $\{T_1, \dots, T_M\}$  **do**  
 Generate  $m$  samples of  $S_{T_j}(\boldsymbol{\theta})$  by the mSOE scheme  
**end for**  
 Compute the loss function  $\mathcal{L}(\boldsymbol{\theta})$  by (3.1) and (3.5)  
 Update  $\boldsymbol{\theta} \leftarrow \boldsymbol{\theta} - \alpha \nabla_{\boldsymbol{\theta}} \mathcal{L}$   
**end while**  
**return**  $\boldsymbol{\theta}$

---

The complete calibration procedure is summarized in Algorithm 1. Compared with existing algorithms for model calibration from option prices, the Wasserstein-1 distance based calibration framework presents the following advantages:

- **Distributional Alignment:** By matching the entire risk-neutral distribution rather than prices at discrete strikes, our method ensures that the calibrated model accurately captures the market-implied dynamics across all strike levels. This is particularly crucial for pricing exotic options whose values depend on the full distribution or path properties, not just terminal payoffs at specific strikes.

- Robustness to Overfitting: The uniform bound interpretation provided by the Kantorovich-Rubinstein duality ensures that our calibration objective controls pricing errors across all possible strikes, not just those included in the calibration set. This inherent regularization makes the method particularly robust and reduces overfitting to potentially noisy price observations.
- Computational Tractability through Monte Carlo: The "simulate-and-compare" paradigm enabled by our efficient mSOE scheme, circumvents the need for closed-form pricing formulas. This makes the framework applicable to broad class of complex models where analytical or fast numerical pricing is unavailable. The empirical Wasserstein distance between one-dimensional distributions is computationally efficient, which only requires  $\mathcal{O}(m \log(m))$  operations per evaluation.
- Favorable Optimization Landscape: As we will demonstrate empirically in Section 4.2.3, the Wasserstein-1 distance as the loss function yields smoother and more convex optimization landscapes compared to traditional metrics like MSE. The improved landscape facilitates more stable convergence, reduces sensitivity to initialization and enhances the reliability of the calibration process.

**Remark 3.1.** *For synthetic data, the market-implied distribution  $S_T^{MKT}$  is readily available by the mSOE scheme since we could prespecify the ground truth model parameters. For real market applications, the risk-neutral distribution can be extracted from option prices, see [11] for a review of this direction.*

## 4 Numerical tests

This section presents a comprehensive numerical evaluation of the proposed mSOE scheme and the Wasserstein-1 distance-based calibration algorithm. We first assess the numerical accuracy and convergence properties of the mSOE scheme against the SOE scheme, examining both implied volatility smiles and surfaces. Subsequently, we demonstrate the performance of the calibration framework, highlighting its generalization capability and parameter identifiability compared to the conventional MSE approach.

### 4.1 Numerical accuracy of the mSOE scheme

#### 4.1.1 European call option

We commence our numerical assessment by evaluating the performance of the mSOE scheme in pricing European call options. The model parameters are specified as follows [7]

$$S_0 = 1, \quad \xi_0(t) = 0.235^2, \quad H = 0.07, \quad \rho = -0.9, \quad \eta = 1.9, \quad (4.1)$$

with a maturity  $T = 1$  and a set of 21 log-strikes  $k_i = -0.55 + 0.05 \times i$  for  $i = 1, \dots, 21$ . A reference implied volatility smile is computed via the exact Cholesky factorization [6], serving as the benchmark. The performance of the proposed mSOE scheme is compared against the SOE scheme detailed in [4, Section 4.3]. For both SOE and mSOE scheme, the

nodes  $\{\lambda_k\}$  and weights  $\{\omega_k\}$  for the sum-of-exponentials approximation are determined using the method introduced in [17, Section 2]. Specific values for varying numbers of summation terms  $N$  are provided in Table 2. An additional objective is to numerically investigate the convergence rates of these schemes as the number of steps  $n$  increases.

Figure 1 displays the implied volatility smiles generated by the Cholesky factorization, SOE, and mSOE scheme for a fixed number of time steps  $n = 128$ . The SOE scheme exhibits minor deviations from the benchmark for at-the-money strikes and significant inaccuracies for out-of-the-money strikes. In contrast, the mSOE scheme effectively mitigates these discrepancies. When  $N = 16$ , the mSOE smile becomes visually indistinguishable from the benchmark and demonstrates its high accuracy.

To numerically determine the convergence rates of the implied volatility smiles, we conduct simulations with a sufficiently large sample size of  $m = 2^{24}$  to minimize Monte Carlo error. Table 3 reports the maximal relative errors over the strike range for both SOE and mSOE schemes, with the results visualized in Figure 2. The SOE scheme fails to exhibit a clear convergent pattern as  $n$  increases. Conversely, the mSOE scheme demonstrates stable convergence across different values of  $N$ . As illustrated in Figure 3, the convergence rate of the mSOE scheme improves with an increasing number of summation terms  $N$ .

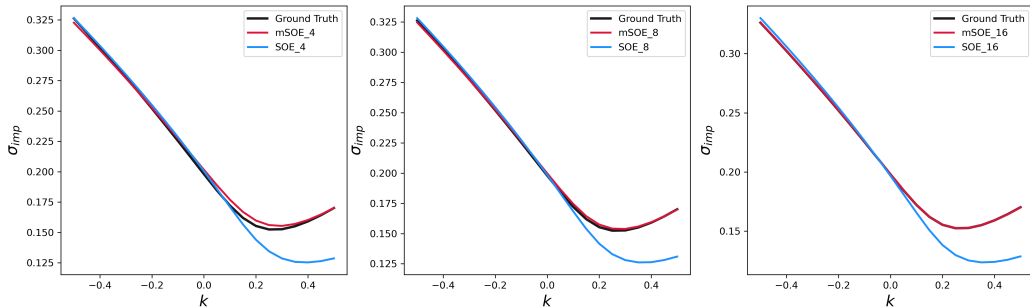


Figure 1: Implied volatility smiles using  $2^{24}$  samples with time steps  $n = 128$ ,  $H = 0.07$ ,  $T = 1$  using nodes and weights given in Table 2 for  $N = 4$  (left),  $N = 8$  (middle) and  $N = 16$  (right).

|          |           |          |           |           |            |            |            |            |
|----------|-----------|----------|-----------|-----------|------------|------------|------------|------------|
| $N = 4$  | $\lambda$ | 0.047108 | 1         | 21.227784 | 450.618823 |            |            |            |
|          | $\omega$  | 0.398569 | 1.482765  | 5.516218  | 20.521561  |            |            |            |
| $N = 8$  | $\lambda$ | 0.161212 | 0.025989  | 0.004190  | 1          | 6.203015   | 38.477401  | 238.675916 |
|          | $\omega$  | 0.404082 | 0.184353  | 0.084107  | 0.885703   | 1.941367   | 4.255266   | 9.327086   |
| $N = 16$ | $\lambda$ | 0.470200 | 0.221072  | 0.102817  | 0.039206   | 0.004176   | 1          | 2.126753   |
|          | $\omega$  | 0.264736 | 0.191490  | 0.145476  | 0.152321   | 0.200620   | 0.366211   | 0.506582   |
|          | $\lambda$ | 9.619464 | 20.458220 | 43.509572 | 92.534093  | 196.797117 | 418.538770 | 890.128395 |
|          | $\omega$  | 0.969363 | 1.340926  | 1.854911  | 2.565910   | 3.549438   | 4.909960   | 6.791977   |
|          |           |          |           |           |            |            |            | 4.395384   |

Table 2: Nodes and weights with varying  $N$ s with  $H = 0.07$ ,  $\tau = 1/128$  and  $T = 1$ .

| $n$  | $N = 4$ |        | $N = 8$ |        | $N = 16$ |        | $N = 32$ |        | $N = 64$ |        |
|------|---------|--------|---------|--------|----------|--------|----------|--------|----------|--------|
|      | SOE     | mSOE   | SOE     | mSOE   | SOE      | mSOE   | SOE      | mSOE   | SOE      | mSOE   |
| 128  | 0.1224  | 0.1617 | 0.1110  | 0.1594 | 0.1277   | 0.1604 | 0.1275   | 0.1629 | 0.1033   | 0.1615 |
| 256  | 0.1685  | 0.0930 | 0.1623  | 0.0918 | 0.1737   | 0.0920 | 0.1492   | 0.0947 | 0.1240   | 0.0951 |
| 512  | 0.2042  | 0.0473 | 0.1820  | 0.0432 | 0.1842   | 0.0451 | 0.1565   | 0.0463 | 0.1414   | 0.0457 |
| 1024 | 0.1448  | 0.0241 | 0.1665  | 0.0150 | 0.1687   | 0.0169 | 0.1474   | 0.0193 | 0.1397   | 0.0178 |
| 2048 | 0.1564  | 0.0148 | 0.1723  | 0.0111 | 0.1471   | 0.0025 | 0.1465   | 0.0027 | 0.1378   | 0.0021 |

Table 3: Maximal relative error (over strikes) for the implied volatility smiles with  $H = 0.07$ ,  $T = 1$  and  $m = 2^{24}$ .

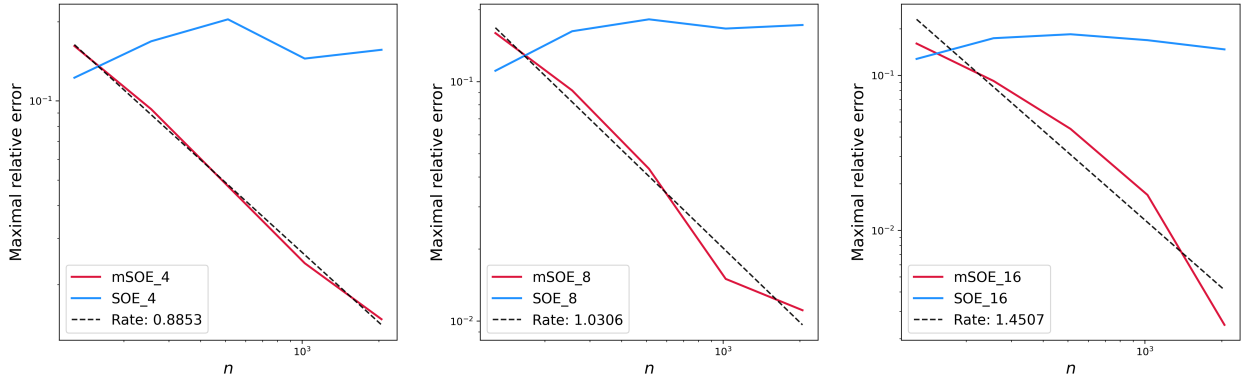


Figure 2: Maximal relative errors of implied volatility smiles using  $m = 2^{24}$  samples with  $H = 0.07$ ,  $T = 1$  and  $N = 4$  (left),  $N = 8$  (middle) and  $N = 16$  (right). The red and blue curves represent the maximal errors over strikes between the true smile and the smile obtained by the mSOE and SOE schemes, respectively. The black dashed lines give a reference for the weak convergence rates with varying  $N$ s.

#### 4.1.2 Implied volatility surface

We now examine the performance of schemes in recovering the entire implied volatility surface, utilizing the same set of model parameters as in (4.1). The maturities and log-strikes are given as

$$T_j = \frac{j}{8}, \quad \mathbf{k}_j = [-0.1, -0.09, \dots, 0.05] \times \sqrt{T_j}, \quad j = 1, 2, \dots, 8.$$

The results are summarized in Table 4 and depicted in Figure 4, which fundamentally align with the findings for the volatility smiles. The SOE scheme fails to converge consistently with increasing  $n$ , whereas the mSOE scheme exhibits stable convergence behavior with its rate enhancing as  $N$  increases, as shown in Figure 5.

## 4.2 Calibration by Wasserstein-1 distance

In this subsection, we demonstrate the performance of the proposed calibration framework outlined in Algorithm 1. To isolate the impact of the loss function itself, we adopt a simplified setup where all model parameters  $(\xi_0, H, \rho, \eta)$  are treated as scalar trainable variables. This

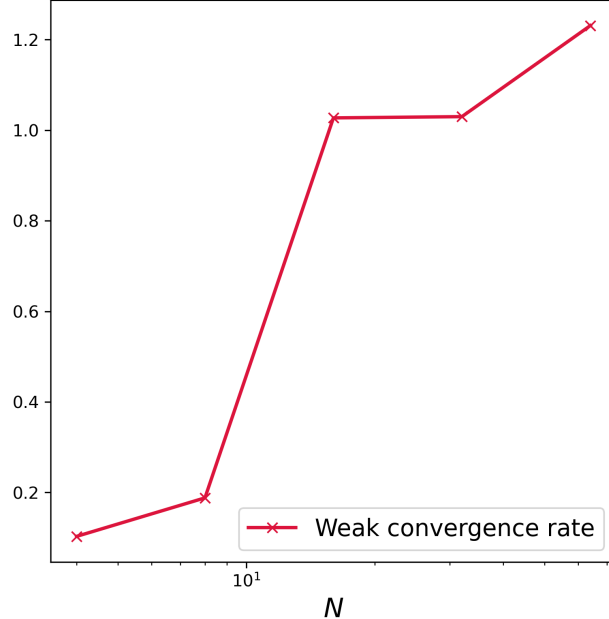


Figure 3: Weak convergence rate of maximal relative errors of implied volatility smiles for the mSOE scheme with varying  $N$ s.

| $n$  | $N = 4$ |        | $N = 8$ |        | $N = 16$ |        | $N = 32$ |        | $N = 64$ |        |
|------|---------|--------|---------|--------|----------|--------|----------|--------|----------|--------|
|      | SOE     | mSOE   | SOE     | mSOE   | SOE      | mSOE   | SOE      | mSOE   | SOE      | mSOE   |
| 128  | 0.0123  | 0.0249 | 0.0092  | 0.0140 | 0.0172   | 0.0157 | 0.0175   | 0.0155 | 0.0168   | 0.0148 |
| 256  | 0.0117  | 0.0258 | 0.0070  | 0.0127 | 0.0196   | 0.0079 | 0.0190   | 0.0079 | 0.0173   | 0.0087 |
| 512  | 0.0108  | 0.0253 | 0.0091  | 0.0127 | 0.0202   | 0.0040 | 0.0191   | 0.0044 | 0.0185   | 0.0040 |
| 1024 | 0.0092  | 0.0196 | 0.0116  | 0.0091 | 0.0195   | 0.0012 | 0.0185   | 0.0020 | 0.0176   | 0.0019 |
| 2048 | 0.0100  | 0.0200 | 0.0122  | 0.0087 | 0.0172   | 0.0012 | 0.0184   | 0.0009 | 0.0173   | 0.0004 |

Table 4: Maximal relative error (over maturities and strikes) for the implied volatility surface, with  $H = 0.07$  and number of samples  $2^{24}$ .

allows any observed performance differences to be attributed directly to the choice of loss function. We conduct the calibration process under four distinct parameter scenarios, as listed in Table 5. Case 0 serves as the benchmark. Case 1 features a lower volatility level, Case 2 alters the roughness parameter, and Case 3 modifies the correlation and volatility-of-volatility level. The initial guess  $\boldsymbol{\theta}_{\text{init}}$  for each case is generated by applying a fixed vector of relative deviation rates  $\mathbf{r}$  to the ground truth parameters  $\boldsymbol{\theta}_{\text{true}}$ , ensuring all experiments start from a consistent level of prior knowledge.

The maturities and strikes used for training and testing are specified in Table 6. The training set for each maturity includes four at-the-money and slightly out-of-the-money options, representing the most liquid segment of the market. Deep out-of-the-money options are intentionally excluded from the training set but are included in the test set to evaluate the model's tail-pricing generalization.

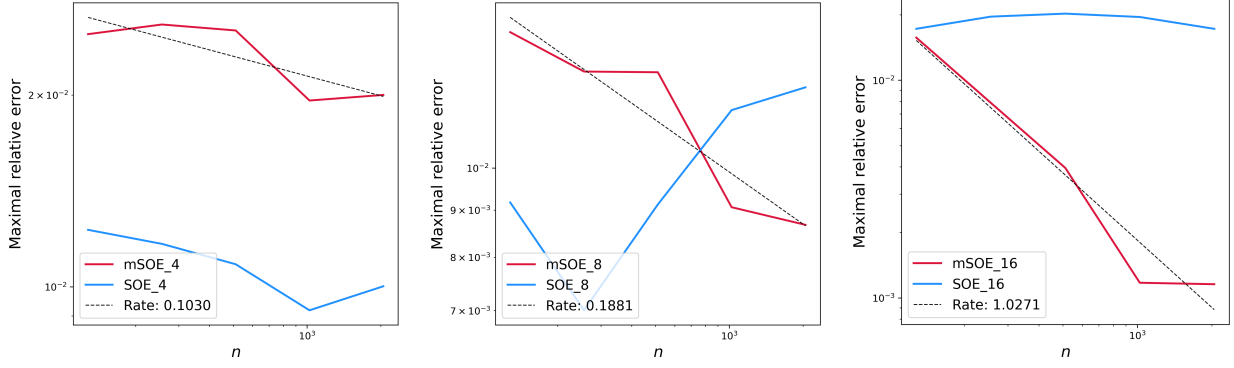


Figure 4: Maximal relative errors of implied volatility surfaces using  $m = 2^{24}$  samples with  $H = 0.07$  and  $N = 4$  (left),  $N = 8$  (middle) and  $N = 16$  (right). The red and blue curves represent the maximal errors between the true surface and surfaces obtained by the mSOE and SOE schemes, respectively. The black dashed lines give a reference for the convergence rates with varying  $N$ .

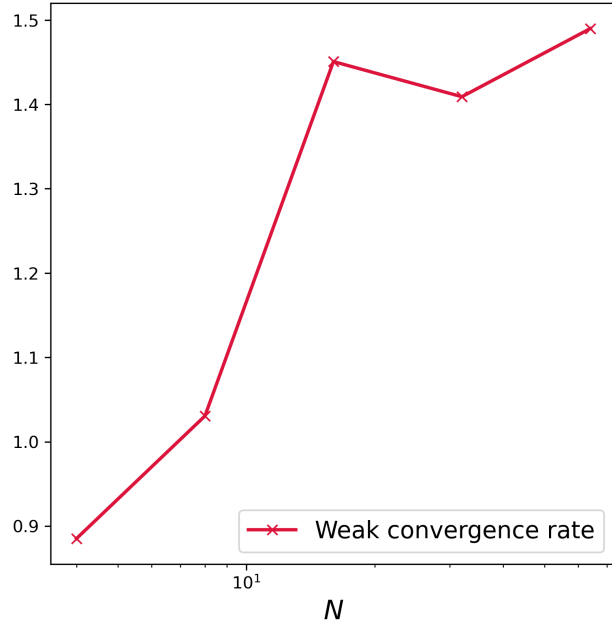


Figure 5: Weak convergence rate of maximal relative errors of implied volatility surface for the mSOE scheme with varying  $N$ s.

#### 4.2.1 Calibration with European Options

The calibration results for European put and call options are summarized in Table 7. The third and fourth columns report the average time per iteration and the total number of iterations completed, respectively. The in-sample pricing errors are presented in columns 5-8, while the out-of-sample errors are shown in columns 9-12. We define the following error

|        |                                     | $\xi_0(t)$ | $H$   | $\rho$ | $\eta$ |
|--------|-------------------------------------|------------|-------|--------|--------|
| Case 0 | $\boldsymbol{\theta}_{\text{true}}$ | 0.09       | 0.07  | -0.9   | 1.9    |
|        | $\boldsymbol{\theta}_{\text{init}}$ | 0.15       | 0.12  | -0.7   | 1.5    |
| Case 1 | $\boldsymbol{\theta}_{\text{true}}$ | 0.04       | 0.07  | -0.9   | 1.9    |
|        | $\boldsymbol{\theta}_{\text{init}}$ | 0.067      | 0.12  | -0.7   | 1.5    |
| Case 2 | $\boldsymbol{\theta}_{\text{true}}$ | 0.09       | 0.02  | -0.9   | 1.9    |
|        | $\boldsymbol{\theta}_{\text{init}}$ | 0.15       | 0.034 | -0.7   | 1.5    |
| Case 3 | $\boldsymbol{\theta}_{\text{true}}$ | 0.09       | 0.07  | -0.7   | 2.2    |
|        | $\boldsymbol{\theta}_{\text{init}}$ | 0.15       | 0.12  | -0.544 | 1.737  |

Table 5: The set of ground truth  $\boldsymbol{\theta}_{\text{true}}$  and the initial guess  $\boldsymbol{\theta}_{\text{init}}$  of model parameters.

|                  |                       |  |
|------------------|-----------------------|--|
| $\boldsymbol{T}$ | train set<br>test set | [0.3, 0.5, 1.0]                                  |
| $\boldsymbol{K}$ | train set<br>test set | [0.9, 0.95, 1.0, 1.05]<br>[0.8, 0.85, 1.1, 1.15] |

Table 6: The set of maturities and strikes used for training and testing.

metrics:

$$\begin{aligned} \text{RMSE} &= \sqrt{\frac{1}{M} \sum_{j=1}^M (P_j(\boldsymbol{\theta}^*) - P_j(\boldsymbol{\theta}_{\text{true}}))^2}, & \text{MAE} &= \frac{1}{M} \sum_{j=1}^M |P_j(\boldsymbol{\theta}^*) - P_j(\boldsymbol{\theta}_{\text{true}})|, \\ \text{MAPE} &= \frac{1}{M} \sum_{j=1}^M \left| \frac{P_j(\boldsymbol{\theta}^*) - P_j(\boldsymbol{\theta}_{\text{true}})}{P_j(\boldsymbol{\theta}_{\text{true}})} \right|, & \text{MaxAPE} &= \max_{j=1, \dots, M} \left\{ \left| \frac{P_j(\boldsymbol{\theta}^*) - P_j(\boldsymbol{\theta}_{\text{true}})}{P_j(\boldsymbol{\theta}_{\text{true}})} \right| \right\}, \end{aligned}$$

where  $\boldsymbol{\theta}^*$  is the set of parameters output by the calibration algorithm. To compute the benchmark prices ( $P_j(\boldsymbol{\theta}_{\text{true}})$ ) and get the market-implied samples required by Algorithm 1, samples of ( $S_{T_j}(\boldsymbol{\theta}_{\text{true}})$ ) are generated using the mSOE scheme with the following setting:

$$\tau = 1/1000, \quad \varepsilon = 10^{-4}, \quad \text{MC repetition} = 2^{14}. \quad (4.2)$$

The same setting is used during optimization to generate samples ( $S_{T_j}(\boldsymbol{\theta})$ ) and compute ( $P_j(\boldsymbol{\theta})$ ). Note that the number of summation terms  $N$  adapts at each iteration based on the current  $H$  to maintain the prescribed precision  $\varepsilon$ . The optimization termination criteria are set as  $\epsilon_{\text{wass}} = 10^{-4}$  for the Wasserstein-1 distance and  $\epsilon_{\text{mse}} = 10^{-8}$  for the MSE. We employ TensorFlow [1] as the autodifferentiable framework and Adam optimizer with piecewise decaying learning rates. For Wasserstein-1 distance, the learning rate is set to  $\alpha = 0.001$  for the first 800 iterations, and is 0.0002 thereafter; for MSE, it is 0.003 for the first 20 iterations and is 0.001 afterwards. The patience for Wasserstein-1 distance is 80 iterations and 40 for MSE. We set the minimum tolerable loss improvement to be  $\Delta_{\text{wass}}^{\min} = 10^{-5}$  and  $\Delta_{\text{mse}}^{\min} = 10^{-9}$ .

As evidenced in Table 7, our proposed calibration algorithm utilizing the Wasserstein-1 distance significantly outperforms the MSE-based approach in both accuracy and efficiency. The Wasserstein-1 distance reduces in-sample errors by approximately an order of magnitude

across all error metrics and achieves out-of-sample errors that are one or two orders of magnitude lower than those of MSE. Moreover, Wasserstein-1 distance attains these calibration results with considerably fewer iterations and a comparable time per iteration, which indicates a more favorable loss landscape that facilitates convergence to a high quality solution. The absolute percentage errors (APE) between the calibrated and ground truth parameters,

|        |               | Training      |        | in-sample |           |           |        | out-of-sample |           |        |        |
|--------|---------------|---------------|--------|-----------|-----------|-----------|--------|---------------|-----------|--------|--------|
|        |               | Time (s/Iter) | # Iter | RMSE      | MAE       | MAPE      | MaxAPE | RMSE          | MAE       | MAPE   | MaxAPE |
| Case 0 | MSE           | 12.6879       | 4428   | 9.9998e-5 | 7.7059e-5 | 0.0017    | 0.0078 | 0.0005        | 0.0004    | 0.0245 | 0.1041 |
|        | Wasserstein-1 | 12.6296       | 784    | 7.3206e-6 | 5.8081e-6 | 0.0001    | 0.0002 | 9.1872e-6     | 7.6096e-6 | 0.0003 | 0.0006 |
| Case 1 | MSE           | 18.8615       | 2701   | 9.9992e-5 | 8.0785e-5 | 0.0033    | 0.0164 | 0.0005        | 0.0004    | 0.0994 | 0.5137 |
|        | Wasserstein-1 | 12.8750       | 727    | 1.2026e-5 | 1.1676e-5 | 0.0004    | 0.0009 | 1.0937e-5     | 1.0289e-5 | 0.0016 | 0.0055 |
| Case 2 | MSE           | 17.6240       | 4900   | 0.0001    | 9.9951e-5 | 0.0015    | 0.0044 | 0.0003        | 0.0002    | 0.0103 | 0.0383 |
|        | Wasserstein-1 | 13.0066       | 2414   | 4.8257e-6 | 4.0039e-6 | 7.0847e-5 | 0.0002 | 5.8467e-6     | 5.4562e-6 | 0.0002 | 0.0007 |
| Case 3 | MSE           | 13.8499       | 4999   | 0.0002    | 0.0001    | 0.0030    | 0.0110 | 0.0007        | 0.0005    | 0.0293 | 0.1148 |
|        | Wasserstein-1 | 12.6730       | 1281   | 6.9588e-6 | 5.7244e-6 | 0.0001    | 0.0005 | 9.8498e-6     | 8.8244e-6 | 0.0005 | 0.0012 |

Table 7: The calibration performance comparison between MSE and Wasserstein-1 distance as loss functions.

defined as

$$APE = \left| \frac{\theta^* - \theta_{\text{true}}}{\theta_{\text{true}}} \right|,$$

are presented in Table 8. The method based on the Wasserstein-1 distance accurately recovers all four model parameters under all scenarios, which confirms its strong parameter identifiability. In contrast, despite the MSE-based method minimizes in-sample pricing errors, its learned parameters exhibited substantial deviations from true values. These results underscore that distributional matching via the Wasserstein-1 distance effectively mitigates overfitting and robustly identifies the data-generating process compared with pointwise price matching with MSE.

|        | APE           | $\xi_0(t)$ | $H$       | $\rho$    | $\eta$    |
|--------|---------------|------------|-----------|-----------|-----------|
| Case 0 | MSE           | 0.0385     | 0.1709    | 0.0448    | 0.1523    |
|        | Wasserstein-1 | 0.0003     | 0.0016    | 0.0002    | 0.0004    |
| Case 1 | MSE           | 0.0364     | 0.2330    | 0.0375    | 0.1644    |
|        | Wasserstein-1 | 1.0259e-3  | 1.1836e-3 | 3.1696e-5 | 1.5984e-3 |
| Case 2 | MSE           | 0.0165     | 0.1704    | 0.0100    | 0.1709    |
|        | Wasserstein-1 | 3.0270e-4  | 9.0992e-4 | 9.3354e-5 | 1.6407e-3 |
| Case 3 | MSE           | 0.0429     | 0.3689    | 0.0006    | 0.1578    |
|        | Wasserstein-1 | 0.0010     | 0.0007    | 0.0002    | 0.0014    |

Table 8: Absolute percentage error between  $\theta_{\text{true}}$  and  $\theta^*$ .

#### 4.2.2 Generalization to Barrier Options

To further evaluate the calibrated model’s capacity to capture the tail behavior of the underlying asset’s distribution, we design experiments involving barrier options. These options are

particularly sensitive to the dynamics and extremes of the asset price path, which provides a stringent test beyond the European options used in calibration. We focus on two types which target opposite tails of the distribution:

1. Left-tail test: Down-and-Out Put (DOP) Option

A DOP has a payoff identical to a standard European put option, conditional upon the underlying asset price not breaching a lower barrier level  $B$  from above during the option's lifetime. Its payoff function is formally defined as:

$$h_{\text{DOP}}(S_T) = \begin{cases} \max(K - S_T, 0), & \text{if } \min_{t \in [0, T]} S_t > B, \\ 0, & \text{otherwise.} \end{cases}$$

This instrument is highly sensitive to the left-tail risk (downside movement) of the underlying distribution.

2. Right-tail test: Up-and-Out Call (UOC) Option

A UOC acts like a standard call option if the asset price never rises above the barrier  $B$  and "knocks out" otherwise. Its payoff function is given by

$$h_{\text{UOC}}(S_T) = \begin{cases} \max(S_T - K, 0), & \text{if } \max_{t \in [0, T]} S_t < B, \\ 0, & \text{otherwise.} \end{cases}$$

This option tests the model's accuracy in capturing the right-tail risk (upside movement).

The contract parameters for the DOP and UOC tests are detailed in Table 9. To rigorously assess the model's generalization capability, the barrier levels  $B$  are deliberately set outside the range of strikes that are used for calibration in Table 6. Figure 6 presents the prices of

|              | DOP                         | UOC                         |
|--------------|-----------------------------|-----------------------------|
| $\mathbf{T}$ | $[0.3, 0.5, 1.0]$           |                             |
| $\mathbf{K}$ | 0.95                        | 1.05                        |
| $\mathbf{B}$ | $[0.70, 0.71, \dots, 0.85]$ | $[1.15, 1.16, \dots, 1.30]$ |

Table 9: The contract parameters of barrier options.

DOP and UOC options computed using the model parameters calibrated in Case 1 over a range of barrier levels. The results consistently demonstrate that the pricing curves generated by the Wasserstein-1 distance calibrated parameters (red) are nearly indistinguishable from the benchmark (black) across all maturities and barrier levels. This verifies the exceptional accuracy and robustness of our calibration method in pricing path-dependent exotic options.

In contrast, prices derived from the MSE-calibrated parameters (blue) exhibit significant and systematic biases. This is particularly pronounced for UOC options, where the MSE model consistently overvalues the contracts. This systematic mispricing is directly attributable to an inaccurate representation of the underlying distribution's tails. As visualized in the log-density plots of  $S_T$  in Figure 7, the MSE model underestimates the probability mass

in the right tail. Consequently, it underestimates the likelihood of the asset price reaching the UOC barrier, leading to an overvaluation of the option by assigning a too low probability to the knock-out event.

#### 4.2.3 Loss landscape

To elucidate the optimization behaviours of different loss functions, we visualize the two-dimensional loss landscapes for the model parameters  $(\xi_0, H, \rho, \eta)$  using the Wasserstein-1 distance in Figure 8 and the MSE in Figure 9. The contour plots are generated by evaluating the losses over a  $25 \times 25$  grid for each parameter pair, with values log-transformed for clarity. Same setting as (4.2) is employed for the simulation and option pricing. The red star marks the true parameter values in Case 0, Table 5. The yellow circle denotes the empirical minimum from the numerical grid search.

Observe that the MSE landscapes exhibit irregular valleys and sharp curvature variations, particularly for the pairs  $(\xi_0, H)$ ,  $(\xi_0, \eta)$  and  $(H, \eta)$ . Such patterns suggest a rugged optimization landscape, which contains multiple local minima and narrow basins. In contrast, the landscapes of Wasserstein-1 distance appear to be significantly smoother and more convex with more circular contour lines. This structure indicates a more tractable optimization problem. Furthermore, the tilted elliptical contours in some MSE panels suggest strong correlations among learned parameters. However, the more symmetric contours in Wasserstein-1 landscapes indicate a reduced level of parameter coupling, which enhances parameter identifiability. This analysis confirms that the Wasserstein-1 distance provides a more favorable loss landscape, which explains the improved convergence reliability and robustness observed in the calibration experiments.

### 4.3 Learning $\xi_0(t)$ with neural networks

Finally, we investigate the capability of the calibration framework to learn the time-dependent initial forward variance curve  $\xi_0(t)$  using three different parameterizations.

1. Piecewise constant (PWC) function: a flexible, non-parametric approach where the target function is defined on a set of maturity pillars  $\{T_0, T_2, \dots, T_L\}$  covering the range  $[0, T]$ :

$$\xi_0^{\text{PWC-}L}(t) = \sum_{l=1}^L \theta_l \mathbb{1}_{[T_{l-1}, T_l)}(t),$$

where the trainable values  $\boldsymbol{\theta}_\xi = (\theta_1, \theta_2, \dots, \theta_L)$ .

2. Nelson-Siegel (NS) model: a parsimonious parametric model widely used in interest rate modeling [20]:

$$\xi_0^{\text{NS}}(t) = \beta_0 + \beta_1 \exp\left(-\frac{t}{\tau}\right) + \beta_2 \left(\frac{t}{\tau}\right) \exp\left(-\frac{t}{\tau}\right),$$

where  $\boldsymbol{\theta}_\xi = (\beta_0, \beta_1, \beta_2, \tau)$ .

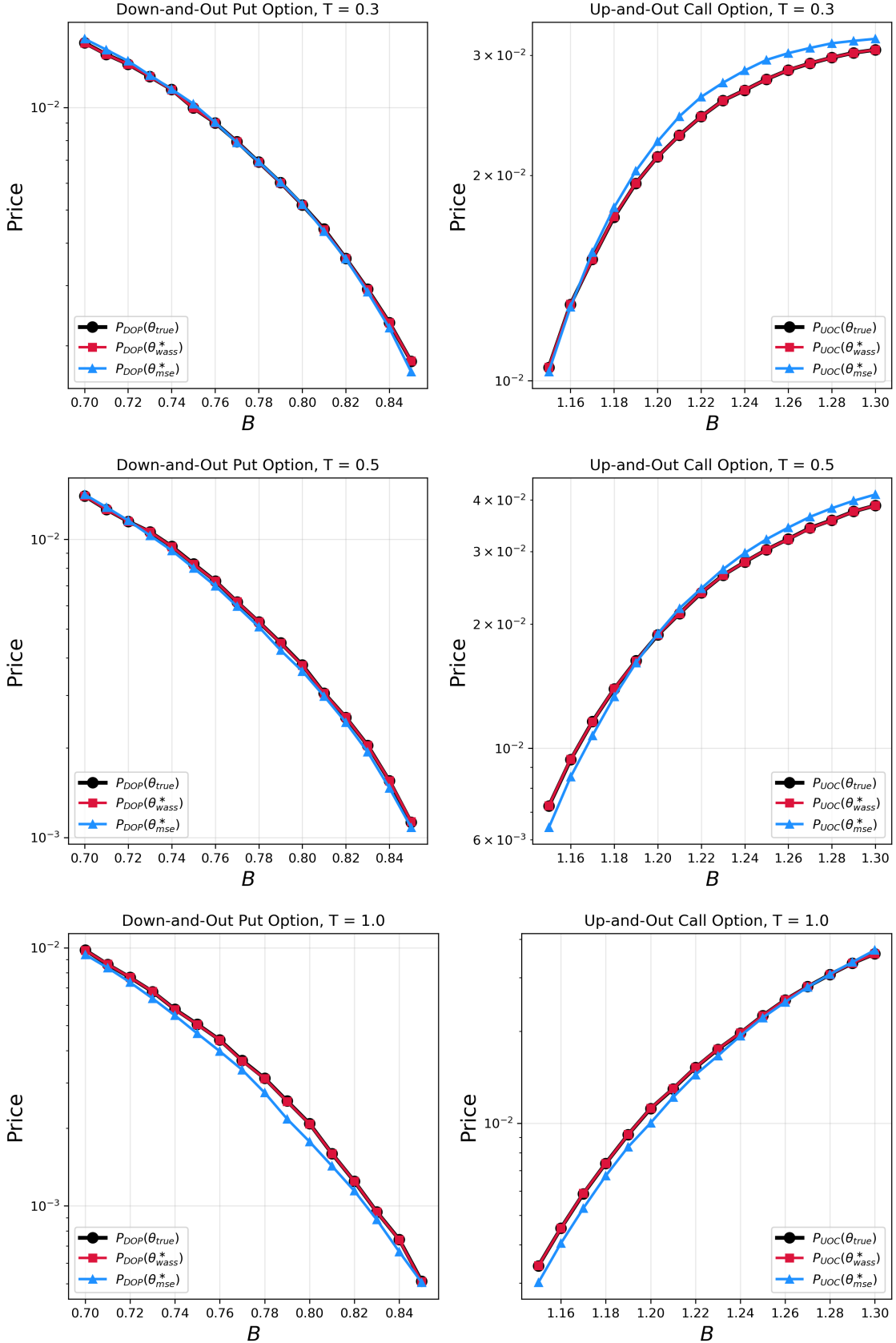


Figure 6: From top to bottom: the price of DOP and UOC options based on different model parameters at  $T = 0.3, 0.5, 1.0$ .

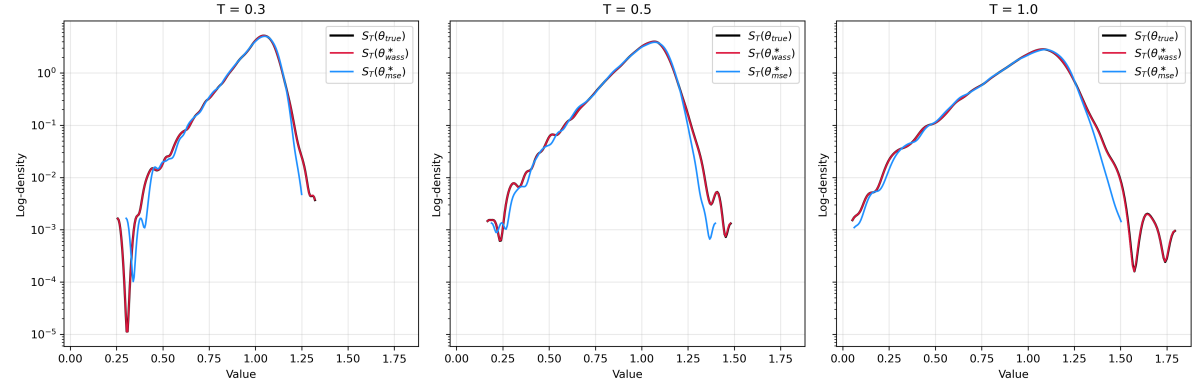


Figure 7: From left to right: the log density plot of future states at  $T = 0.3, 0.5, 1.0$  using Gaussian kernel estimation with  $2^{14}$  samples.

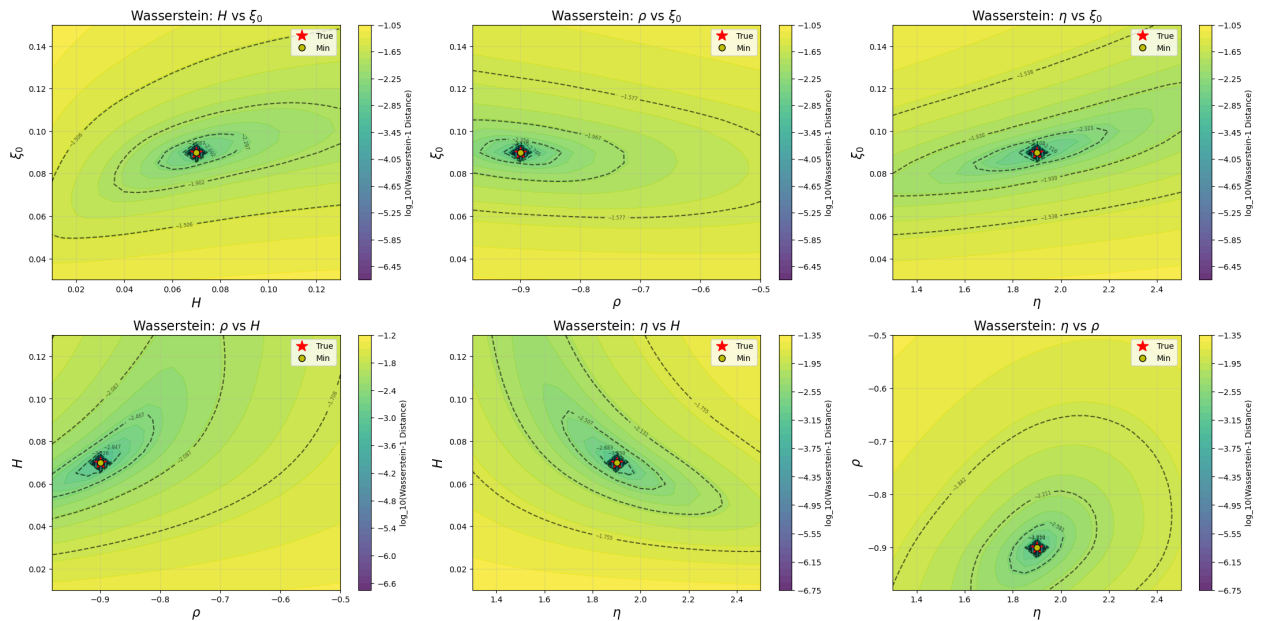


Figure 8: Contour plot of Wasserstein-1 distance.

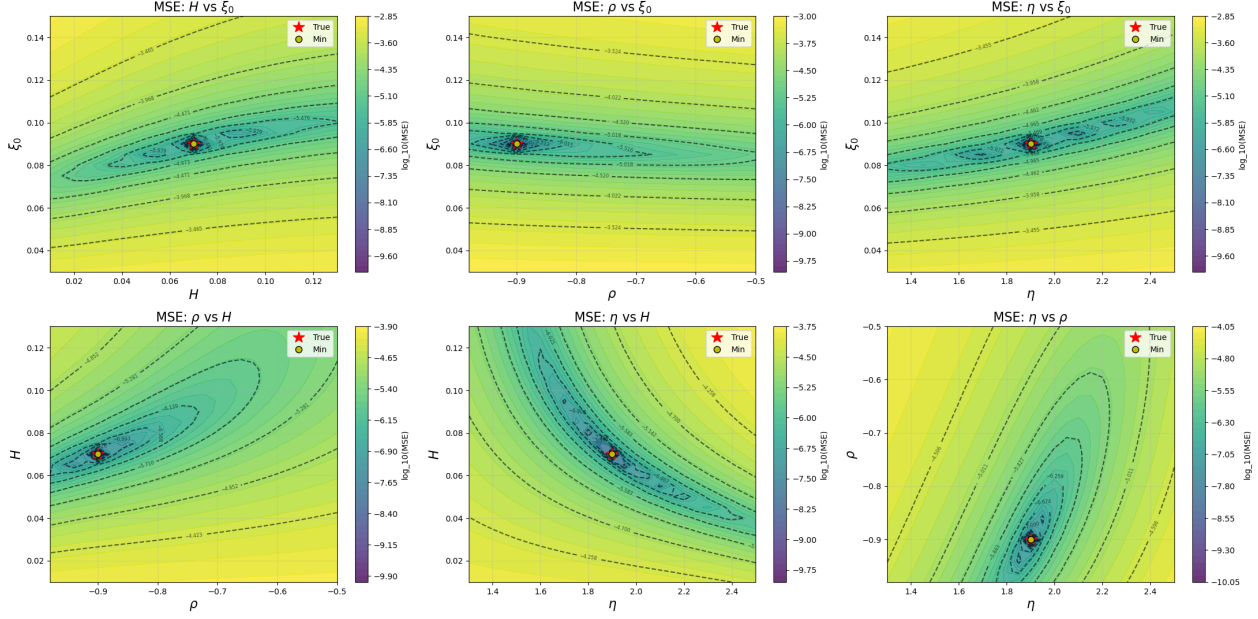


Figure 9: Contour plot of MSE.

3. Neural network-enhanced Nelson-Siegel model: to combine the structural prior of the NS model with the universal approximation capability of neural networks, we use a small neural network to learn a residual correction to the NS model

$$\xi_0^{\text{NS+NN}}(t) = |\xi_0^{\text{NS}}(t)(1 + \kappa \mathcal{NN}(t; \mathbf{w}))|,$$

where the trainable parameters  $\boldsymbol{\theta}_\xi = (\beta_0, \beta_1, \beta_2, \tau, \kappa, \mathbf{w})$  include the NS parameters, the scaling factor  $\kappa$  and neural network weights  $\mathbf{w}$ . The network  $\mathcal{NN}(t; \mathbf{w})$  takes time  $t$  as input and outputs a correction term. We use a simple architecture with 2 hidden layers of 8 units each and leaky ReLU activation functions. The absolute form ensures the positivity of the initial forward variance curve.

To evaluate these parameterizations, we define three distinct ground truth curves for  $\xi_0(t)$ , moving beyond simple constant or monotonic shapes:

$$\begin{aligned} \xi_0^{(1)}(t) &= 0.05 \exp(-t), \\ \xi_0^{(2)}(t) &= 0.02 + 0.03 \exp(-5t) + 3t \exp(-5t), \\ \xi_0^{(3)}(t) &= 0.03 + 0.05 \exp(-5(t - 0.3)^2) + 0.01 \sin(15t), \end{aligned} \tag{4.3}$$

where  $\xi_0^{(1)}$  tests the ability to capture a simple and smooth decay,  $\xi_0^{(2)}$  is exactly a Nelson and Siegel curve with parameters  $(\beta_0, \beta_1, \beta_2, \tau) = (0.02, 0.03, 0.6, 0.2)$ , and  $\xi_0^{(3)}$  is a highly oscillatory function with a localized hump. The other model parameters are fixed at the benchmark values from Case 0, Table 5. The initial guesses for the parameters of each method are provided in Table 10. The set of maturities and strikes used for this experiment is detailed in Table 11. Samples of the underlying price process generated at each iteration

obey the following setting:

$$\tau = 1/1000, \quad \varepsilon = 10^{-4}, \quad \text{MC repetition} = 2^{17}.$$

The calibration process will be early stopped with patience 30 and  $\Delta^{\min} = 10^{-5}$ .

| PWC-8 |  | 0.05   |
|-------|--|--|
| NS    |  | $\beta_0 = 0.03, \beta_1 = 0.02, \beta_2 = 0.15, \tau = 0.15$                |
| NS+NN |  | $\beta_0 = 0.03, \beta_1 = 0.02, \beta_2 = 0.15, \tau = 0.15, \kappa = 0.01$ |

Table 10: The initial guess of different parameterizations.

|              |           |  |
|--------------|-----------|--|
| $\mathbf{T}$ | train set | [0.3, 0.5, 1.0]                              |
|              | test set  | [1.2, 1.5]                                   |
| $\mathbf{K}$ | train set | [0.8, 0.85, 0.9, 0.95, 1.0, 1.05, 1.1, 1.15] |
|              | test set  |  |

Table 11: The set of maturities and strikes used for the in-sample and out-of-sample error metrics computation.

The calibration results are summarized in Table 12 and the learned curves are visualized in Figure 10. The PWC parameterization consistently achieves the lowest in-sample pricing errors across all three curves. Its flexibility allows it to adapt closely to diverse functional forms, but it lacks inherent smoothness and generalization capability to the maturities outside of the training range. For the NS case, it performs excellently if the true curve lies within its functional form, as indicated from the case of  $\xi_0^{(2)}(t)$ . However, it fails to adequately capture the shapes of  $\xi_0^{(1)}(t)$  and  $\xi_0^{(3)}(t)$  and leads to higher pricing errors. For the neural network-enhanced parameterization, it has mild improvements for both in-sample and out-of-sample performance compared with the pure NS case. This indicates that neural network plays a very limited role for the expressive enhancement and generalization.

|                  |       | Training      |         | in-sample |           |        |        | out-of-sample |        |        |        |
|------------------|-------|---------------|---------|-----------|-----------|--------|--------|---------------|--------|--------|--------|
|                  |       | Time (s/Iter) | # Iters | RMSE      | MAE       | MAPE   | MaxAPE | RMSE          | MAE    | MAPE   | MaxAPE |
| $\xi_0^{(1)}(t)$ | PWC-8 | 14.0561       | 172     | 8.7270e-5 | 7.0621e-5 | 0.0046 | 0.0150 | 0.0017        | 0.0015 | 0.0543 | 0.1455 |
|                  | NS    | 13.8007       | 596     | 0.0002    | 0.0001    | 0.0116 | 0.0667 |               |        |        |        |
|                  | NS+NN | 13.8025       | 643     | 0.0002    | 0.0001    | 0.0116 | 0.0661 |               |        |        |        |
| $\xi_0^{(2)}(t)$ | PWC-8 | 13.8567       | 1069    | 0.0004    | 0.0003    | 0.0063 | 0.0230 | 0.0015        | 0.0013 | 0.0153 | 0.0335 |
|                  | NS    | 14.0246       | 3188    | 0.0002    | 0.0002    | 0.0027 | 0.0099 |               |        |        |        |
|                  | NS+NN | 13.8616       | 1048    | 0.0003    | 0.0002    | 0.0042 | 0.0142 |               |        |        |        |
| $\xi_0^{(3)}(t)$ | PWC-8 | 14.0446       | 99      | 0.0001    | 0.0001    | 0.0037 | 0.0108 | 0.0018        | 0.0018 | 0.0358 | 0.0590 |
|                  | NS    | 14.2029       | 245     | 0.0002    | 0.0002    | 0.0097 | 0.0393 |               |        |        |        |
|                  | NS+NN | 14.2072       | 260     | 0.0002    | 0.0002    | 0.0096 | 0.0390 |               |        |        |        |

Table 12: The performance comparison between different parameterizations of the initial forward variance curve.

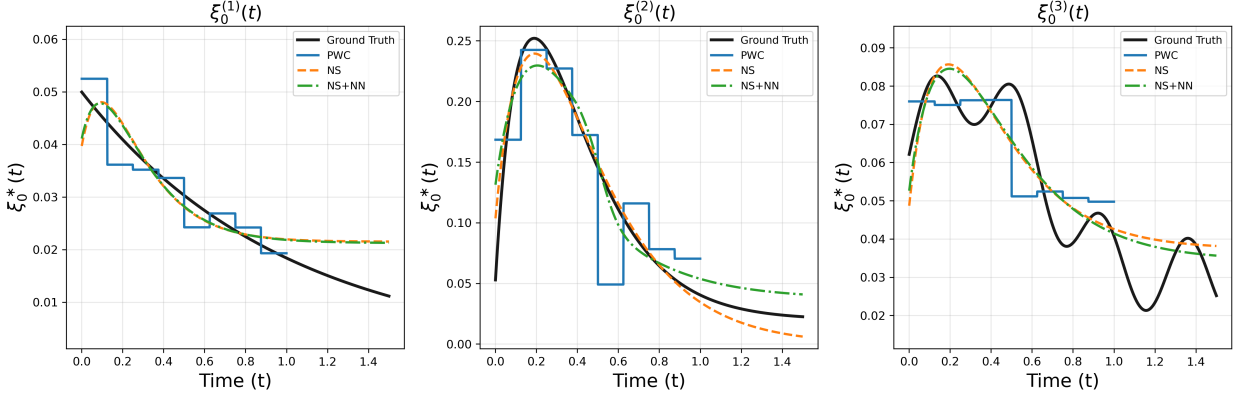


Figure 10: The calibrated  $\xi_0(t)$  using different parameterizations.

## 5 Conclusion

This work introduced a comprehensive framework that addresses the dual challenges of efficient pricing and robust calibration in the rough Bergomi model.

First, we developed a modified Sum-of-Exponentials (mSOE) Monte Carlo scheme by hybridizing an exact treatment of the kernel singularity at the origin with a high-fidelity sum-of-exponentials approximation for the remainder. Our method achieves stable convergence and high accuracy, particularly for out-of-the-money options, compared with the SOE scheme. It maintains an  $\mathcal{O}(n)$  computational complexity, which makes it a practical and efficient pricing engine.

Second, we proposed a novel calibration paradigm based on distributional matching via the Wasserstein-1 distance, which minimizes the distance between the model-generated and market-implied risk-neutral distributions. It provides a uniform bound on pricing errors over all strikes and corresponds to an adversarial optimization over Lipschitz payoffs. Extensive numerical tests confirm that this framework yields superior parameter identifiability and exceptional generalization capability to exotic options such as barrier options, compared to the traditional mean squared error approach. The "simulate-and-compare" paradigm, enabled by our efficient mSOE pricer, makes this a generic and powerful tool for calibrating complex models where fast analytical pricing is unavailable.

Finally, we demonstrated the flexibility of the calibration framework by incorporating different parameterizations for the initial forward variance curve  $\xi_0(t)$ . This allows the model to adapt to various term structure shapes present in market data.

Future work will focus on several promising directions. The most immediate extension is the application of our framework to real market data. This involves extracting the market-implied risk-neutral distribution from option price quotes to compute the empirical Wasserstein distance. Furthermore, the generic nature of our calibration framework invites its application to other rough and non-Markovian models beyond rBergomi.

## Acknowledgements

GL acknowledges the support from GRF (project number: 17317122) and the Early Career Scheme (Project number: 27301921), RGC, Hong Kong.

## References

- [1] M. Abadi, P. Barham, J. Chen, Z. Chen, A. Davis, J. Dean, M. Devin, S. Ghemawat, G. Irving, M. Isard, et al. Tensorflow: a system for large-scale machine learning. In *12th USENIX symposium on operating systems design and implementation (OSDI 16)*, pages 265–283, 2016.
- [2] E. Abi Jaber and O. El Euch. Multifactor approximation of rough volatility models. *SIAM Journal on Financial Mathematics*, 10(2):309–349, 2019.
- [3] F. Baschetti, G. Bormetti, and P. Rossi. Deep calibration with random grids. *Quantitative Finance*, pages 1–23, 2024.
- [4] C. Bayer and S. Breneis. Markovian approximations of stochastic Volterra equations with the fractional kernel. *Quantitative Finance*, 23(1):53–70, 2023.
- [5] C. Bayer and S. Breneis. Weak Markovian approximations of rough Heston. *arXiv preprint arXiv:2309.07023*, 2023.
- [6] C. Bayer, P. Friz, and J. Gatheral. Pricing under rough volatility. *Quantitative Finance*, 16(6):887–904, 2016.
- [7] M. Bennedsen, A. Lunde, and M. S. Pakkanen. Hybrid scheme for Brownian semistationary processes. *Finance and Stochastics*, 21:931–965, 2017.
- [8] D. Braess. *Nonlinear approximation theory*. Springer Science & Business Media, 2012.
- [9] M. De Angelis and A. Gray. Why the 1-Wasserstein distance is the area between the two marginal cdfs. *arXiv preprint arXiv:2111.03570*, 2021.
- [10] T. DeLise. Neural options pricing. Preprint, arXiv:2105.13320, 2021.
- [11] S. Figlewski. Risk-neutral densities: A review. *Annual Review of Financial Economics*, 10(1):329–359, 2018.
- [12] P. Gassiat. On the martingale property in the rough Bergomi model. 2019.
- [13] J. Gatheral, T. Jaisson, and M. Rosenbaum. Volatility is rough. In *Commodities*, pages 659–690. Chapman and Hall/CRC, 2022.
- [14] A. Gulisashvili. Gaussian stochastic volatility models: Scaling regimes, large deviations, and moment explosions. *Stochastic Processes and their Applications*, 130(6):3648–3686, 2020.

- [15] P. Harms. Strong convergence rates for Markovian representations of fractional Brownian motion, 2019.
- [16] B. Horvath, A. Muguruza, and M. Tomas. Deep learning volatility: a deep neural network perspective on pricing and calibration in (rough) volatility models. *Quantitative Finance*, 21(1):11–27, 2021.
- [17] S. Jiang, J. Zhang, Q. Zhang, and Z. Zhang. Fast evaluation of the Caputo fractional derivative and its applications to fractional diffusion equations. *Communications in Computational Physics*, 21(3):650–678, 2017.
- [18] P. Kidger, J. Foster, X. Li, and T. J. Lyons. Neural SDEs as infinite-dimensional GANs. In *International conference on machine learning*, pages 5453–5463. PMLR, 2021.
- [19] S. Liu, A. Borovykh, L. A. Grzelak, and C. W. Oosterlee. A neural network-based framework for financial model calibration. *Journal of Mathematics in Industry*, 9(1):9, 2019.
- [20] C. R. Nelson and A. F. Siegel. Parsimonious modeling of yield curves. *Journal of business*, pages 473–489, 1987.
- [21] S. E. Rømer. Hybrid multifactor scheme for stochastic Volterra equations with completely monotone kernels. Available at SSRN 3706253, 2022.
- [22] A. Tong, T. Nguyen-Tang, T. Tran, and J. Choi. Learning fractional white noises in neural stochastic differential equations. In *Advances in Neural Information Processing Systems*, volume 35, pages 37660–37675, 2022.
- [23] C. Villani. *Topics in optimal transportation*. American Mathematical Soc., Providence, 2021.
- [24] D. V. Widder. *The Laplace Transform*, volume vol. 6 of *Princeton Mathematical Series*. Princeton University Press, Princeton, NJ, 1941.
- [25] Q. Zhu, G. Loeper, W. Chen, and N. Langrené. Markovian approximation of the rough Bergomi model for Monte Carlo option pricing. *Mathematics*, 9(5):528, 2021.